Tuning the Pr valence state to design high oxygen mobility, redox and transport properties in the CeO2-ZrO2-PrOx phase diagram

Vincent Frizon, Jean-Marc. Bassat, Michaël Pollet, Etienne Durand, Julien Hernandez, Karine Pajot, Philippe Vernoux, Alain Demourgues

Tuning the Pr Valence State to Design High Oxygen Mobility, Redox and Transport Properties in the CeO_2-ZrO_2-PrO_x Phase Diagram

Vincent Frizon[,+,Θ], Jean-Marc Bassat[,+], Michael Pollet[,+], Etienne Durand[,+], Julien Hernandez[$], Karine Pajot[¥], Philippe Vernoux[Θ] and Alain Demourgues*[,+]

[,+] : CNRS, Université de Bordeaux, ICMCB, 87 avenue du Dr. Albert Schweitzer, 33608 Pessac, France
$: SOLVAY, RIC, 52 rue de la Haie Coq, 93308 Aubervilliers Cedex, France
¥ : 78943 Vélizy-Villacoublay
Θ : IRCELYON, 2 avenue Albert Einstein, F-69626, Villeurbanne Cedex, France

* : Corresponding author

ABSTRACT: The preparation and characterization of pure fluorite-type phases allowed exploring the CeO_2-ZrO_2-PrO_x (CZP) phase diagram. On the basis of magnetic susceptibility measurements, the Pr^{4+}/Pr^{3+} molar ratio of several oxides annealed at T=700°C under air was determined; the higher the Zr content, the lower the Pr^{4+} concentration. Thermogravimetric Analysis (TGA) and Temperature Programmed Reduction (TPR) measurements showed the various Pr and Ce reduction steps. The Pr^{4+} reduction starts at T=250°C and is maximum around T=400°C. For the most reducible compositions, which exhibit the lowest Zr content and the highest Pr rate, the reduction phenomena strongly depend on the Pr/Ce molar ratio. As a remarkable result, Pr and Ce reduction can simultaneously take place at lower temperature (T>430°C) than for oxides of the CeO_2-ZrO_2 solid solution evidencing that the increase of Pr content also allows enhancing the reducibility of Ce^{4+} at low temperature. On the basis of a discussion taking into account a probability of oxygen surroundings in disordered fluorite networks, and the released oxygen rate in materials after the first reduction step performed at T<500°C, a mapping of the most probable labile oxygen sites in the CZP phase diagram is proposed. In particular, it is shown that for the oxides containing 10% Zr at., the most labile oxygen site should be systematically coordinated with one Zr atom, one Ce and two Pr atoms. In the same series (10% Zr at.), electronic transport properties allowed showing semi-conducting behavior with a strong increase of the total conductivity as the Pr content raises. On the basis of the thermal variation of the Seebeck coefficient, these phenomena are associated to electrons and holes hopping, involving intra-atomic charge transfers which depend on the reduction temperature of Pr^{4+} ions under air. Finally, the oxygen mobility strongly increases with the Pr content in this series. The oxygen tracer self-diffusion coefficient D* has been estimated by two independent measurements and the best value is around 10^{-8} $cm^2.s^{-1}$ at T=400°C for the $Ce_{0.45}Zr_{0.1}Pr_{0.45}O_{2-x}$ composition, which is quite high in this temperature range. These fundamental properties of CZP phases design very promising new materials like automotive exhaust catalysts, gas sensors, electrolytes or oxygen electrodes for solid oxide fuel cells.

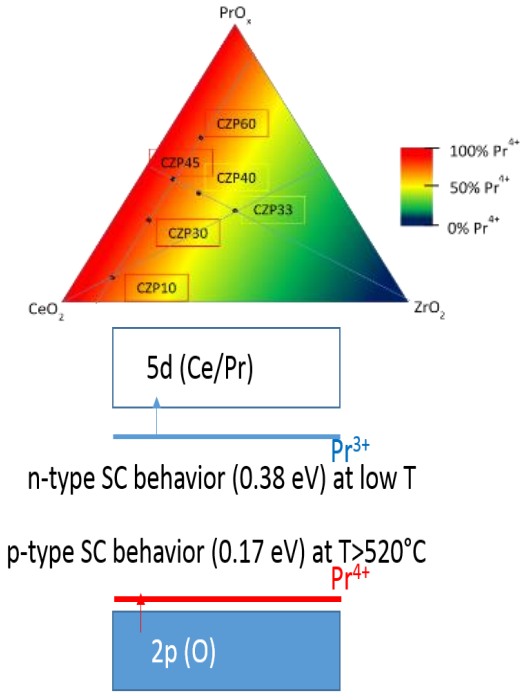

INTRODUCTION. In the last 20 years, intensive efforts have dealt with the environmental impact decrease of the automotive exhaust gases. Cerium-based oxides, deemed as oxygen buffers, have been widely investigated as key components for Three Way Catalysts (TWCs, stoichiometric air-fuel mixture), Diesel soot abatement (Lean-burn conditions) and wet oxidation[1,2,3,4,5]. Ceria-Zirconia mixed oxides materials have been developed as TWCs[1]. They exhibit high Oxygen Storage Capacity (OSC) with high oxygen release under reducing conditions, fast kinetics, high content of reducible Ce^{4+} at T<600°C, and high thermal stability with rather good surface areas (between 20 and 40 m^2/g) stabilized at T> 1000°C[6]. Various crystallographic lattices such as fluorite-type for high Ce rate, tetragonal distortion of fluorite-type structure for Zr-rich phases and pyrochlore-type structure for equimolar compositions have been characterized for the last 20 years[6,7,8]. The pyrochlore corresponds to a fluorite-type superstructure including both $Ce^{4+}$and Ce^{3+}, eight-fold coordinated to oxygens, and Zr^{4+} cations located in a distorted octahedral site as well as oxygen vacancies ordering. The

corresponding materials have the best redox properties[6,7,8,9,10]. Cations sites distortions as well as cationic ordering play a key role for OSC, Ce reducibility and minimum temperature of reduction.

Praseodymium-based oxides should be able to compete with Cerium-based ones [11]. As compared to Ce, Pr has one electron more in its shell, and Pr^{4+} appears both less stable and more reducible than Ce^{4+} (with respect to their respective ionization energies); in addition, the redox potential of Pr^{4+}/Pr^{3+} in solution is larger (2.7 V/ENH) than that of Ce^{4+}/Ce^{3+} (1.7 V/ENH). This elements then easily appears with a mixed valence state combining Pr^{4+} and Pr^{3+}. For instance its most stable stoichiometric compounds are Pr_7O_{12} or $Pr_{24}O_{44}$ (Pr_6O_{11}). The Pr_nO_{2n-2m} series was extensively studied by Eyring *et al*[11,12,13].

The $Pr_{1-x}Zr_xO_{2-y}$ solid solution has already been investigated[14]; the materials exhibit mixed valence states associated to oxygen vacancies with redox processes occurring at low temperature. In these compounds, the higher the Zr content, the lower the Pr valence state: the larger Pr^{3+}-O^{2-} bond is compensated by the smaller Zr^{4+}-O^{2-} bond distance while simultaneously oxygen vacancies are formed. The Zr^{4+} ions stabilization in distorted octahedral site is at the origin of the formation of stoichiometric compositions stabilizing the oxygen vacancies in a fluorite-type structure. In particular, it was evidenced that in the Pr-rich compounds[14], high amounts of Pr^{4+} ions could be reduced under air even at low temperature (T<250°C). In addition, the fluorite-type superstructure (SG : *Ia-3*) of reduced compositions (T=900°C under Ar/5%H_2) exhibits both a cationic and oxygen vacancies ordering: Zr^{4+} cations are stabilized in flattened octahedral sites allowing the formation of oxygen vacancies and the stabilization of Pr^{3+}.

Following this work, a CeO_2 incorporation in the Pr-rich compounds ($Pr_{1-x}Zr_xO_{2-y}$, x≤0.5) has been investigated[15,16]. Zr-rich compounds (Zr molar content between 0.55 and 0.75) exhibit the best thermal stability with high OSC for low Pr rate (between 0.03 and 0.10) [15,16]. At lower Zr content, the $Zr_{0.1}(Ce_{1-x}Pr_x)_{0.9}O_{2-y}$ solid solution offers an optimal OSC with a bell curve peaking for x=0.5 and the oxygen vacancies rate, associated to Pr^{4+}/Pr^{3+} molar ratio, should be responsible for these enhanced OSCs[22]. Indeed, the OSC is closely related to both the reducibility and the oxygen mobility, which occurs thanks to the oxygen deficiency allowed by the Pr substitution and the formation of the Pr^{4+}/Pr^{3+} mixed valence state. For Ce-rich oxides (molar rate > 0.66), the Zr substitution leads to a decrease in the total (ionic and electronic) conductivity when p(O_2) decreases. This is associated with a significant reduction of Pr^{4+} to Pr^{3+} in the oxygen impoverished compound with the decrease of the activation energy of the carriers when the compound gains oxygen upon annealing at high temperature [17,18].

However, no information has been given on Pr valence states in the oxidized or reduced phases. The incorporation of 2% Pr into the $Ce_{0.8}Gd_{0.2}O_{1.9}$ network contributes to increase the p-type electronic conductivity by a factor of 3 but no significant changes were observed in the ionic conductivity[19]. Moreover, dealing with $Ce_{1-x}Pr_xO_{2-\delta}$ solid solution (Ce-rich phases), *in-situ* optical absorption and electrochemical impedance spectroscopy show the variation of oxygen non-stoichiometry at elevated temperature and at various p(O_2), leading to follow the optically absorbing center (Pr^{4+}) concentration[20].

Density Functional Theory (DFT) was used to obtain the equilibrium geometries and energies of ceria-based solid solutions[21]. For instance, as the oxygen vacancies were induced in a site directly coordinated with Pd, a strong reduction in the oxygen vacancy formation energy was observed and explained the observed high activity of $Ce_{1-x}Pd_xO_{2-\delta}$ complex oxides for redox reactions[21].

Then, in this series the Pr^{4+}/Pr^{3+} molar ratio appears as a key feature. This work deals with the partial exploration of the CeO_2-ZrO_2-PrO_x phase diagram with a careful control of the Pr^{4+} content, accurately determined from both magnetic measurements and thermogravimetric analysis performed under Ar/5%H_2. In a second step, the reducibility properties involving Pr^{4+} and Ce^{4+} species are discussed. Although the oxygen deficiency is always mentioned as an important parameter in the literature, the identification of labile oxygen and its local environment in its tetrahedral site is hardly ever discussed despite its crucial role for the Oxygen Storage Capacity and mobility properties. Herein, we propose a mapping of the most labile oxygen environment in the CeO_2-ZrO_2-PrO_x outlined phase diagram, using a multinomial law which helps analyzing the oxygen mobility in association with the redox properties.

The temperature dependence of the total conductivity and the Seebeck coefficient has been measured and a schematic band diagram is proposed. The control of Pr^{4+}/Pr^{3+} mixed valences in connection with each composition is shown to allow tuning the transport properties (nature and mobility of the charge carriers).

Finally, the chemical oxygen diffusion coefficients D_{Chem} were determined for the most conductive sample using electronic conductivity relaxation experiments analyzed with a Crank model and isotopic exchange experiments monitored by SIMS analysis.

EXPERIMENTAL SECTION

Several oxides have been prepared starting from nitrates precursors (SOLVAY), co-precipitated in basic medium (pH = 10). At pH=10, all Ce-Zr-Pr hydroxydes and oxyhydroxides precipitate. Precipitates were washed six times with ammonia (M/100) and twice with ethanol followed by a slow drying at T=50°C under air. All these oxides were annealed in air at T=700°C and then at T=1400°C during 12 hours; they crystallize with the fluorite-type structure and no phase transition is observed. All compositions and nomenclature are given in Table1; the samples are named after their cationic composition (*e.g.* CZ contains only Ce and Zr and CZP contains Pr in addition) and their Pr content (*e.g.* CZP60 contains 60 molar% of Pr and 40 molar% of Ce and Zr).

Cation molar ratios were checked with the inductively coupled plasma atomic emission spectroscopy (ICP-AES) technique and correspond to the targeted chemical composition. The samples were first dissolved using hydrochloric acid and heated at 200°C for 15 min using a microwave digestion system (CEM, MARS).

Powder X-Ray diffraction patterns have been collected on a Phillips X'Pert MPD X-ray diffractometer with Bragg-Brentano geometry using Kα1/ Kα2 radiations (8°<2θ<80° step of 0.017 ° and counting time of 60s). Diffractograms have been refined using the Rietveld method and Fullprof package with conventional reliability factors. The unit cell

and profile parameters leading to determine the average crystallite size have been refined. All the diffraction patterns have been indexed on the basis of Fluorite-type structures (SG : Fm-3m).

Surface areas were determined using Brunauer-Emmet-Teller (BET) calculations performed on N_2 adsorption isotherms at T=-196°C, recorded with a Tristar Surface Area and Porosity apparatus from Micromeritics. Outgassing temperature was set at 300°C for all the samples.

Samples for transmission electron microscopy (TEM) were prepared by suspending the powder in alcohol by ultrasonication and depositing a drop of the suspension on a copper grid covered with a carbon film. The grid was finally air-dried for 15 min. TEM, high resolution TEM (HRTEM) and scanning TEM coupled with energy dispersive X-Ray spectroscopy (STEM-EDX) observations were performed using a JEOL 2200 FS equipped with a field emission gun, operating at 200 kV and with a point resolution of 0.23 nm. High-resolution transmission electron microscopy micrographs were acquired with a Gatan Ultrascan CCD 2k - 2k, while digital diffractograms were calculated using the Gatan Digital Micrograph program. Moreover, in order to be representative and statistically meaningful, numerous images from several regions of various samples were recorded and the most characteristic results are presented here.

The thermogravimetric analysis (TGA) have been carried out on SETARAM Setsys evolution under Ar/5% H_2 flux (50 ml/min) with a speed rate of 5°C/min up to T=900°C. TGA experiments have been also carried out under air or Ar up to T=800°C (speed rate: 5°C min for air atmosphere and 3°C/min for Ar atmosphere) for oxides with high Pr content. Samples were pre-treated at T=400°C for 1 hour under O_2 flow (100ml/min) to avoid the partial reduction of the compounds. The same TGA experiments carried out after pre-treatment at T=700°C under air (to remove water/carbonates) into the TGA apparatus, do not influence the temperature and reduction rates in CZP samples. Temperature Programmed Reduction (TPR) have been performed on Micromeritics AutoChemII 2950 HP under Ar/1%H_2 (100 ml/min) up to 800°C (speed rate: 10°C/min) with a mass spectrometer Inficon JPC400 to detect H_2 consumption and H_2O formation. The thermal expansion behavior has been investigated by dilatometry from room temperature to 1400°C under air (speed rate: 5°C/min) on NETZSCH DIL 402C dilatometer.

The Curie constants and θp Weiss temperatures values have been deduced from magnetic susceptibilities measurements ($1/\chi = (T+\theta p)/C$, $\chi = M.H$), the magnetizations being recorded between 125 K and 300 K (speed rate: 10°/min) with a magnetic field of 18000 Oe. Magnetic measurements have been performed on a MicroSense EZ7 vibrating magnetometer. As the Curie constant is proportional to the concentration of the paramagnetic species, the Pr^{3+} ($4f^2$) and Pr^{4+} ($4f^1$) contents in the various compounds can be deduced from magnetic data.

The sintering of uniaxially pressed powders obtained after slow drying at 50°C (see preparation section) allow obtaining dense pellets with a compactness higher than 90%. The temperature variation of the total conductivity has been measured by the four-point probe method which has been carried out from room temperature to 1000 K under air using Pt as contact materials. The total conductivity have been deduced from the R resistance ($1/\sigma$ = R.s/l where s and l are respectively the cross section area and the length of the pellet) by applying electric currents which vary between 0.5 μA and 3 mA. By measuring the voltage difference ΔV between the hot and cold sides of the material versus temperature and the ΔT change in temperature between the two sides, the thermal variation of the Seebeck coefficient $\alpha=\Delta V/\Delta T$ was evaluated.

The oxygen diffusion (D^*) coefficient was determined using dense pellets by the Isotopic Exchange Depth Profile (IEDP) technique combining isotopic exchange of ^{18}O (used as an oxygen tracer) for ^{16}O then Secondary Ion Mass Spectrometry (SIMS) analyses. The complete procedure is detailed in refs[23,24]. Prior to each exchange, a pre-annealing step was performed, which consisted in equilibrating the sample at the temperature of interest (same temperature as the subsequent exchange) in natural ^{16}O oxygen (99.9% purity) at 210 mbar. The time used for the pre-anneal step in natural oxygen was always much longer (at least five times) than the exchange time. Then the sample was exchanged in an ^{18}O enriched gas (97%, Eurisotop) at the same temperature and oxygen partial pressure, for a controlled duration. In order to limit the oxygen stoichiometry change during the heating and cooling ramps, a tubular furnace was rapidly rolled on to set the sample to the annealing temperature and later rolled off to rapidly cool it down. The ^{18}O penetration profiles, *i.e* normalized ^{18}O isotopic fraction (^{18}O / (^{16}O + ^{18}O)), were recorded as a function of the analyzed depth using a Cameca® IMS 6F SIMS apparatus with a Cs^+ ions source. The oxygen profiles were then fitted using an appropriate solution to the diffusion equation given by Crank, for a solution of the second Fick's law of gas diffusion in solids [25].Electrical conductivity relaxation (ECR) measurements were carried out using the four probe method. The pO_2 surrounding the sample was alternatively switched between 0.21 (air) and about $5x10^{-5}$ (Ar) bars. Based on the Crank model[25], the ratio $\frac{M_t}{M_\infty} = \frac{\sigma_t - \sigma_0}{\sigma_\infty - \sigma_0}$, σ_t, σ_0 and σ_∞ being the conductivity values at t, t = 0 and t = ∞, respectively, was fitted, which allowed to model k_{Chem} and D_{Chem}, the chemical surface exchange and diffusion coefficients, respectively.

RESULTS AND DISCUSSION

1-Unit cell parameter, crystallite size, surface area and homogeneity

Raw Diffractograms are plotted in Figure 1 (following annealing at 700°C) and Figure S1 (following annealing at 1400°C). XRD analysis on the samples annealed at 700°C in air allows identifying single phases corresponding to the cubic-fluorite type structure (SG: Fm-3m). In these structures, the small ionic radius of Zr^{4+} is partly compensated by the presence of larger ions such as Pr^{3+} ($r(Pr^{3+})$ = 1.12 Å in eight-fold oxygen-coordinated environment). Nevertheless, the unit-cell parameters, characterizing the powders annealed at 700°C under air, systematically decrease with the zirconium content increase: a (CZP10) = 5.404Å > a (CZP40) = 5.394Å > a (CZP33) = 5.366Å (Table 1). The comparable ionic sizes of Ce^{4+} and Pr^{4+} (respectively equal to 0.99Å and 0.97Å when eight-fold coordinated to oxygen), as well as the occurrence of Pr^{3+} ions may explain the very small differences observed between the unit

cell parameters. In particular, the CZP33 unit-cell parameter (33 molar% Zr) is expected to be significantly lower than that of CZ (20 molar% Zr) but both are almost equal. It can therefore be anticipated that CZP33 oxide contains a non-negligible amount of larger Pr^{3+} ions. The same remark holds between CZ and CZP40 oxides where a larger amount of Pr^{3+} is also expected in the latter case (Table 1).

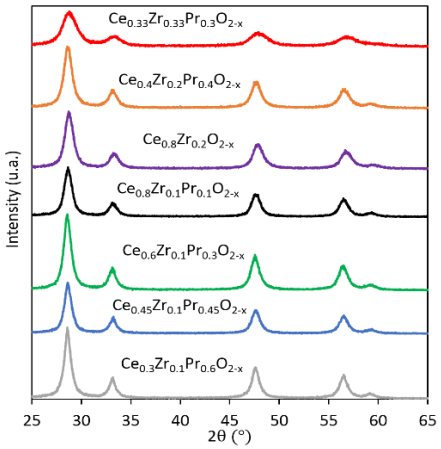

Fig. 1 : Powder XRD patterns of $Ce_{1-x-y}Zr_xPr_yO_{2-z}$ complex oxides annealed at 700°C under air.

Composition	Name	Lattice parameter (Å)	Lattice parameter at 1400°C (Å)	Cristallites size (nm)	Surface area (m^2/g)	Pore size (nm)	Pore volume (cm^3/g)
$Ce_{0.33}Zr_{0.33}Pr_{0.33}O_{2-x}$	CZP33	5.366(3)	5.3593(3)	5(1)	65(1)	4-5	0.20
$Ce_{0.80}Zr_{0.20}O_{2-x}$	CZ	5.372(2)	5.3539(2)	11(1)	84(1)	6-7	0.25
$Ce_{0.40}Zr_{0.20}Pr_{0.40}O_{2-x}$	CZP40	5.394(2)	5.3916(2)	8(1)	34(1)	-	-
$Ce_{0.8}Zr_{0.1}Pr_{0.1}O_{2-x}$	CZP10	5.404(1)	5.3941(1)	9(1)	84(1)	5-6	0.26
$Ce_{0.6}Zr_{0.1}Pr_{0.3}O_{2-x}$	CZP30	5.406(2)	5.3998(1)	9(1)	52(1)	10	0.21
$Ce_{0.45}Zr_{0.1}Pr_{0.45}O_{2-x}$	CZP45	5.404(1)	5.4069(2)	9(1)	47(1)	4-6	0.26
$Ce_{0.3}Zr_{0.1}Pr_{0.6}O_{2-x}$	CZP60	5.402(2)	5.4274(3)	8(1)	41(1)	-	-

Table 1 : Structural and textural characteristics of $Ce_{1-x-y}Zr_xPr_yO_{2-z}$ oxides annealed at 700°C under air.

After annealing at 1400°C, the cell parameter decreases in the Pr-free sample (CZ) and increases in the two most Pr-rich samples (CZP45-60) while it remains almost constant in the other samples. For Pr-free sample, we assume that the significant decrease in the cell parameter (from 5.372(2) Å to 5.3539(2) Å, table 1) should be related to diffusion and cationic reorganization phenomena occurring at high temperature. On the other side, for the Pr-rich samples, the increase in the cell parameter can be associated with a significant increase in the Pr^{3+} concentration after annealing at very high temperatures (reducing conditions). For all other composition a compromise between these two extrema may occur. Note that the reduction from Pr^{4+} to Pr^{3+} is also directly visible on the dilatometry curves (Figure S2) recorded on CZP33 and CZP45 pellets under air with a noticeable shrinkage of the pellets, the one on CZP45 being larger, as expected from the higher Pr content.

It is also important to underline that our synthesis protocol allows producing oxides with crystallites size less than or equal to 10 nm. Zr-rich CZP33, whose diffractogram exhibits the largest HWHM (Figure 1), contains the smallest crystallites (5 nm) in agreement with the results of the literature[3,4,5]. Moreover, it is worth noting that the increase in the Pr rate contributes to a significant reduction of the surface area. On should have to mention that the chemical composition determined by X-ray Photoemission Spectroscopy (XPS, surface information, not presented here) is in very good agreement with the ICP-OES analysis (bulk information, see experimental section)

Since the synthesized materials are monophasic with acceptable surfaces areas and are made up of small crystallites, it is also relevant to check their cationic homogeneity. For this purpose, STEM-EDX measurements were carried out, with the aim to map the different chemical elements over a pre-defined zone, each element being represented by a specific color in Figure.2. The cartographies of Ce, Zr and Pr elements related to the CZP10 and CZP45 compounds are given in Figure S3 (CZP10) and Figure 3 (CZP45), both evidencing a rather good cationic homogeneity.

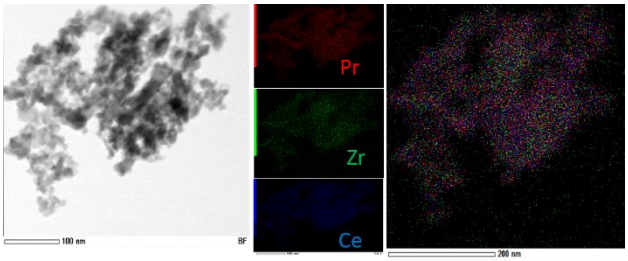

Fig. 2: STEM light field image (left) analysis and EDX elementary analyses of CZP45 complex oxide (right, "three colors" images obtained by addition of the three elementary cartographies).

2-Pr^{4+}/Pr^{3+} molar ratio determined by magnetic measurements in $Ce_{1-x-y}Zr_xPr_yO_{2-z}$ oxides

Only considering the Curie constant, it is impossible to differentiate between Ce^{3+} and Pr^{4+} ions in an oxide with formula $Ce_{1-x-y}Zr_xPr_yO_{2-z}$, both having a $4f^1$ electronic configuration (μ_{eff}= 2.54μ_B, C= 0.806 uem.K/mole). However, as confirmed by thermodynamic considerations[22] and Ellingham diagrams, the Ce^{4+} is stabilized under air atmosphere in fluorite-type structure up to 1600°C. Furthermore, magnetic measurements of $Ce_{1-x}Zr_xO_2$ solid solutions annealed under air at high temperatures show diamagnetic signals and consequently the absence of Ce^{3+}. Therefore, within our experimental measurements conditions (T<400K), we can assume the only presence of a Pr^{4+} / Pr^{3+} mixture and 100% Ce^{4+} so that all Curie constants can be calculated per mole of praseodymium only[26,27,28,29,30,31,32].

Magnetic measurements were performed on the different materials annealed at T=700°C and the linear variation of the reciprocal magnetic susceptibility was plotted versus temperature (see e.g. CZP45 in Figure S4) to extract the Curie constants (Table 2). Taking into account the theoretical effective moments of Pr^{4+} and Pr^{3+} ions (2.54μ_B and 3.58μ_B, respectively, C_{Pr4+}= 0.806 uem.K/mole, C_{Pr3+}= 1.602 uem.K/mole), their proportion can be evaluated for all the $Ce_{1-x-y}Zr_xPr_yO_{2-z}$ series (Table 2 and Figure 3). At low temperature (T<175K), a slight deviation to the Curie-Weiss law must be mentioned leading to consider the more general Van-Vleck formula taking into account the various population of fundamental and excited states and the spin-orbit coupling effect[26-32].

Table 2: Curie constants values, Pr^{4+}/Pr^{3+} molar ratios and Weiss temperature of $Ce_{1-x-y}Zr_xPr_yO_{2-z}$ oxides annealed at 700°C under air, deduced from Curie-Weiss law $1/\chi=(T-\theta p)/C$.

Compositions	$Ce_{0.33}Zr_{0.33}Pr_{0.33}O_{2-x}$	$Ce_{0.40}Zr_{0.20}Pr_{0.40}O_{2-x}$	$Ce_{0.8}Zr_{0.1}Pr_{0.1}O_{2-x}$
Curie constant (uem CGS.K^{-1})	1.250	1.200	1.099
Θ_p (K)	47	81	46
Pr^{4+} (%)	44(1)	51(1)	66(1)
Pr^{3+} (%)	56(1)	49(1)	34(1)
Compositions	$Ce_{0.6}Zr_{0.1}Pr_{0.3}O_{2-x}$	$Ce_{0.45}Zr_{0.1}Pr_{0.45}O_{2-x}$	$Ce_{0.3}Zr_{0.1}Pr_{0.6}O_{2-x}$
Curie constant (uem CGS.K^{-1})	1.078	0.959	1.067
Θ_p (K)	61	40	98
Pr^{4+} (%)	66(1)	81(1)	67(1)
Pr^{3+} (%)	34(1)	19(1)	33(1)

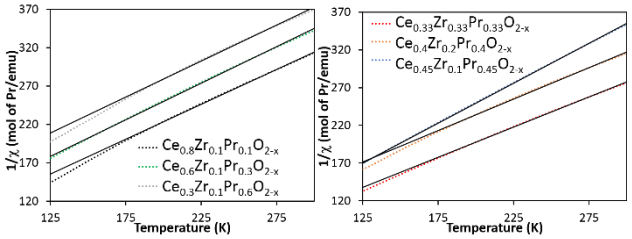

Fig. 3: Temperature dependence of the magnetic susceptibility inverse for the $Ce_{1-x-y}Zr_xPr_yO_{2-z}$ oxides (with constant Zr = 0.1 content, **left,** and variable Zr rate with constant Ce/Pr molar ratio, **right**) annealed at 700°C under air.

Data gathered in Table 2 and plotted in Figure 4 clearly evidence that the lower the Zr rate, the higher the Pr^{4+}content in this series, the only exception being for CZP45 for which the Pr^{4+} proportion peaks at 81% while it is at ca 66% in all other compounds with Zr at 10 molar%. Others CZP compositions (not mentioned in the text) have been prepared and characterized by XRD and magnetic measurements in order to have the best representation of this phase diagram (Figure. 4). Only some representative compounds of the CZP series have been presented and discussed in this manuscript.These results can be globally analyzed in terms of competitive bonds around Zr^{4+} and O^{2-} ions. Zr^{4+} ion is more polarizing than $Ce^{4+}/Pr^{4+}/Pr^{3+}$, because of its lower ionic radius and its higher charge. On the basis of magnetic measurement performed under air at low temperatures, the higher the Zr^{4+} content, the higher the Pr^{3+} rate (the blue color zone on Figure 4), leading to the creation of oxygen vacancies in fluorite-type network. Thus, the larger Pr^{3+}-0^{2-} bond length (more ionic) compensates for the smaller Zr^{4+}-O^{2-} bond distance (more covalent). . The somewhat higher oxidation degree in CZP45 arises from the composition, with equal Ce and Pr concentration, and will be discussed later. The spin interactions as given by the Weiss temperatures are all anti-ferromagnetic but no clear trend emerges from our results.

.

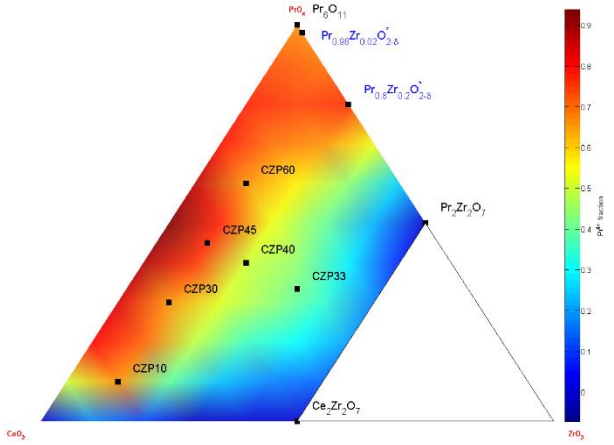

Fig. 4: CeO_2-ZrO_2-PrO_x ternary phase diagram including the studied $Ce_{1-x-y}Zr_xPr_yO_{2-z}$ compositions (CZP). The Pr^{4+}-rich and Pr^{3+}-rich zones are roughly shown. The Pr^{4+}/Pr^{3+} molar ratio has been determined on the basis of magnetic measurements performed on each CZP oxide after annealing at T=700°C under air.

3- Pr^{4+}/Ce^{4+} reduction steps determined by thermogravimetric analysis and temperature programmed reduction

Taking into account the Pr^{4+}/Pr^{3+} molar ratio values previously determined by magnetic measurements, thermogravimetric analysis were performed under $Ar/5\%H_2$ flow in order to estimate the oxygen release related to the Pr^{4+}/Ce^{4+} reduction process. Figure 5 plots the corresponding TGA curves and their derivatives dTG (top graph for compounds containing 20 or 33% at. Zr and the bottom graph for those containing 10% at. Zr). The weight loss at low temperatures (< 300°C) is due to the departure of water molecules and carbonates adsorbed on the powders surface. The materials reduction takes place beyond this temperature, the reduction phenomena occurring by successive waves. By considering the minimum of dTG derivatives, various reduction steps can be identified and quantified. Depending on the composition, one to three main reduction steps can be more or less easily evidenced. The weight losses, change in stoichiometry and evolution of RE^{4+}/RE^{3+} rare earth molar ratios data, are reported in Table S1. For each compound, these data are given during the three reduction steps: 300°C <T <500°C, then up to 700°C and finally up to 900°C. The same starting hypothesis was used than for the magnetic titration: cerium is solely considered as Ce^{4+} in the pristine materials before reduction. Then the stoichiometry of CZP33 before TGA experiment is $Ce_{0.33}Zr_{0.33}Pr_{0.33}O_{1.9}$ and becomes $Ce_{0.33}Zr_{0.33}Pr_{0.33}O_{1.84}$ after reduction at 470°C. At this temperature, 10% of the Pr ions remain at the oxidation state +4. At 700 ° C, all the Pr ions are in the trivalent state and the reduction of Ce^{4+} to Ce^{3+} begins. At 900°C, 63% of the cerium are in the trivalent state, and the composition of CZP33 oxide is finally $Ce_{0.33}Zr_{0.33}Pr_{0.33}O_{1.72}$. Considering CZP40, CZP10 and CZP30, all Pr^{4+} ions are reduced during the first reduction step at low temperatures.

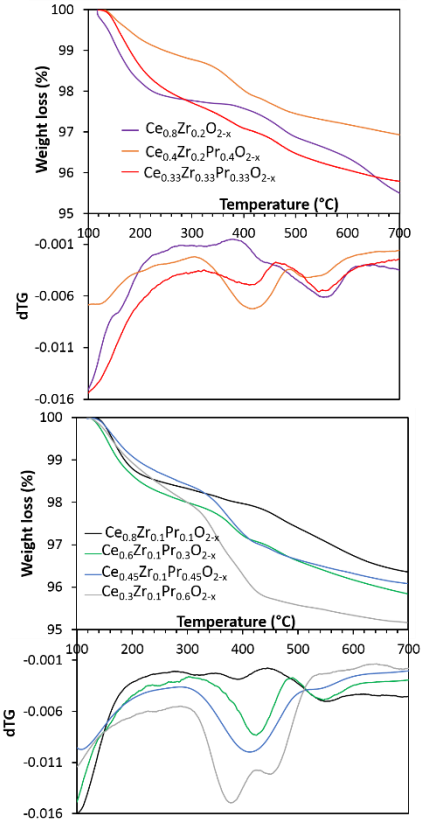

Fig. 5 : Thermogravimetric curve (TG) and first derivative curve (dTG) obtained for the $Ce_{1-x-y}Zr_xPr_yO_{2-z}$ compounds annealed at 700°C under air and reduced under Ar/5% H_2 atmosphere (Ramp temperature = 5°C/min. Total flow = 50 cm^3/min).

For CZP45 and CZP60 compounds, at least 11% of Pr remains as tetravalent state after the first reduction step. These two oxides being also the most reducible in this temperature range, their high praseodymium content could explain this result. Finally, CZ (without praseodymium) begins to reduce at a higher temperature (380°C) than the other ones and only 5% of cerium is reduced during the first reduction stage between 380°C and 455°C. Therefore, it can be concluded that the introduction of Pr into the $Ce_{1-x}Zr_xO_{2-z}$ networks greatly improves the reducibility for temperatures below 500°C. By investigating the reducibility of $Ce_{1-x-y}Zr_xPr_yO_{2-z}$ with a constant Zr content of 0.1 (see Figure 5), the reducibility increases with increasing praseodymium levels, both at low temperature and over the entire range of temperature. Taking into account the percentage of oxygen release, the following classification can be proposed regarding the first low temperature reduction step (T<500°C, Table 3): CZP10 (%O = 3) < CZP30 (%O = 8) < CZP45 (%O = 10.5) < CZP60 (%O = 13). Similarly, the total reducibility follows the same classification (from Table 3): CZP10 (%O = 11) < CZP30 (%O = 14.5) < CZP45 (%O = 15) < CZP60 (%O = 20.5).

Table 3: ΔO released rate before (initial) and during TGA (TGA, Ar/5% H_2) (compounds annealed at T = 700 °C under air, see table 1 for oxides formulae).

Oxides	ΔO	%O (=ΔO/2*100)	Total %O
CZP33	ΔO inital 0.1	5	13
	0.06 (320-470°C)	3	
	0.08 (470-700°C)	3	
	0.04 (700-900°C)	2	
CZ	ΔO inital 0	0	9.5
	0.04 (380-500°C)	2	
	0.09 (500-700°C)	4.5	
	0.06 (700-900°C)	3	
CZP40	ΔO initial 0.1	5	14.5
	0.09 (305-490°C)	4.5	
	0.06 (490-700°C)	3	
	0.04 (700-900°C)	2	
CZP10	ΔO inital 0.02	1	11
	0.04 (310-460°C)	2	
	0.1 (460-700°C)	5	
	0.06 (700-900°C)	3	
CZP30	ΔO inital 0.06	3	14.5
	0.1 (305-490°C)	5	
	0.08 (490-700°C)	4	
	0.05 (700-900°C)	2.5	
CZP45	ΔO inital 0.05	2.5	15
	0.16 (300-520°C)	8	
	0.05 (520-700°C)	2.5	
	0.04 (700-900°C)	2	
CZP60	ΔO initial 0.1	5	20.5
	0.16 (290-430°C)	8	
	0.09 (430-540°C)	4.5	
	0.03 (540-700°C)	1.5	
	0.03 (700-900°C)	1.5	

Starting with Pr^{4+}/Pr^{3+} molar ratio determined by magnetic measurements for samples annealed at T=700°C under air, the ΔO released oxygen rate at moderate temperature (300°C-500°C) under reducing atmosphere have been estimated (reported on Tables 3 and 1-SI) on the basis of TGA experiments. Thus, it seems clear that the majority of Pr^{4+} ions is then reduced in a first step (between 300°C and 500 °C) as clearly illustrated in Figure 5. Only CZP45 containing the highest Pr^{4+} rate (81%) undergoes a reduction of Pr^{4+} above 500°C accompanied by that of the Ce^{4+} ions. For CZ and CZP40 compounds (both containing 20% at.% Zr), the percentage of reducible Ce^{4+} in the second stage (up to 700 ° C) is almost identical (about 30%). As Zr content increases (CZP33), this reducible Ce^{4+} level increases, demonstrating the influence of Zr which allows enhancing the Ce^{4+} reducibility independently of that of Pr^{4+} ions. For the same Ce and Pr content but when decreasing the Zr atomic ratio (comparison between CZP40 and CZP45), the two reduction phenomena associated to Pr and Ce are well differentiated. For instance, the Pr-rich CZP60 oxide exhibits an interesting behavior with two reduction phenomena occurring at low temperature. The first one occurs between 300°C and 450°C, where about 90% of Pr^{4+} ions are reduced, and the next one occurs

between 450°C and 550°C, which contributes to the reduction of 10% of remaining Pr^{4+} and 30% of Ce^{4+}. Considering a constant Zr content (for instance 10% at Zr in Table 3), the first reduction is initiated at a lower temperature as the Pr rate is high, confirming that in the presence of Ce and Zr atoms, the Pr^{4+} ions within the fluorine network are highly reducible.

Finally, the increase of Zr and Pr concentrations allows raising the Pr^{3+} rate associated to oxygen vacancies and the Ce^{4+} reducible rate at low temperature. Thus, the occurrence of large polarizable cations (Pr^{3+}) associated to oxygen vacancies and smaller polarizing cations (Zr^{4+}) strongly contribute to disturb the local environment of labile oxygen.

Figure 6 shows the H_2-TPR profiles of CZ, CZP10, CZP33 and CZP45 oxides annealed at 700°C. The total hydrogen uptakes, calculated from the area measured between T = 30°C and 800°C are given in Table 1-SI. The reduction appears globally lower than within the TGA experiments because of the less reductive setup (1%H_2 for TPR and 5%H_2 for TGA). The reducibility at low temperatures (350°C<T<500°C) of CZP10 is slightly higher than that of CZ oxide but it is the opposite for T>500°C. The total reducibility of CZ compound (497 µmol/g) is greater than that of CZP10 oxide, which is 345 µmol/g. Two reduction peaks are evidenced in CZP10.

The reduction starts at much lower temperatures, around 250°C, for CZP33. Two reduction peaks can be clearly distinguished at 440°C and around 610°C, slightly shifted from CZP10 oxide (containing less Pr and Zr but more Ce).

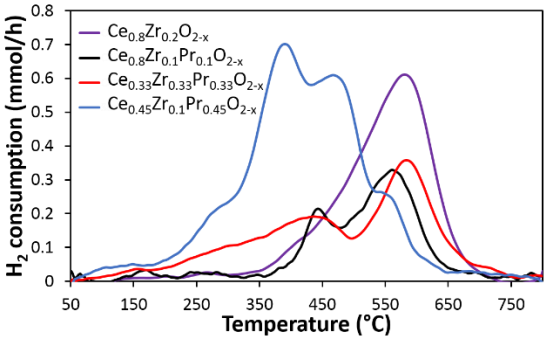

Fig. 6: H_2-TPR analysis of selected $Ce_{1-x-y}Zr_xPr_yO_{2-z}$ complex oxides annealed at 700°C under air and reduced under Ar/1% H_2 atmosphere. Ramp temperature = 10°C/min. Total flow = 100 cm^3/min.

The total consumption of hydrogen is the same as that of CZ oxide. On the other hand, its reducibility at low temperatures is much higher. It is therefore jointly the increase in the Pr and Zr contents which contributes to raise the reducibility at low temperature in agreement with the thermogravimetric analysis presented above.

Finally, this TPR analysis allows identifying the different reduction phenomena in good agreement with the TGA experiments: i) at very low temperatures, the reduction of surface Pr^{4+} ions may first occur[1,2,3,4,5,6]; ii) from about 300°C to 520°C, two stages of Pr^{4+} reduction are evidenced on the basis of TGA (first derivative) curves, possibly in link with two different labile oxygen sites within the fluorite network, as discussed in the next section, iii) the TGA curve of CZP60 compound, a Pr-rich compound like CZP45 phase, also reveals the occurrence of two reduction steps between 300°C and 500°C.

4- Discussion around the labile oxygen site on the basis of a statistical approach

MO_2 fluorite can be described as a 3D lattice[1] of edge sharing tetrahedrons of the cations surrounding the oxygen ions. Assuming an ideal statistical distribution of the cations in all the compounds under study, we discuss the impact of the local environment of the oxygen on its lability and the reducibility of the compounds. The analysis is based on the results of magnetic measurements, which determine the room temperature oxygen non-stoichiometry after the synthesis under air at 700 °C, and the TGA measurements in a reductive atmosphere, which give its evolution with temperature. As shown in Figure 7 in the cases of CZP60-45-30, the derivatives of the TGA curves highlight several domains and, in the following, we will assume that they represent the activation of some specific oxygen sites depending on their cation environment.

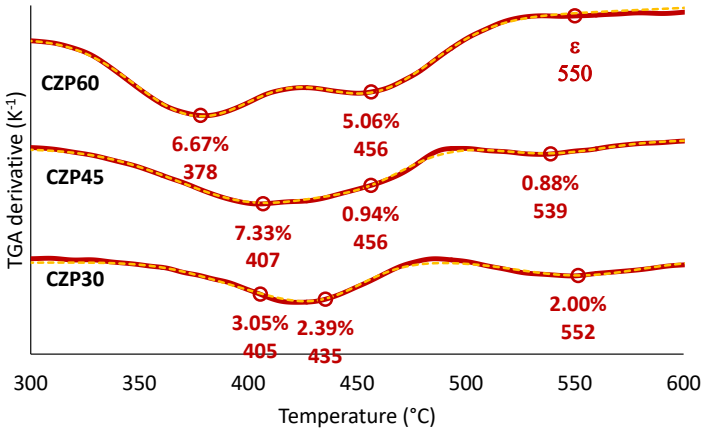

Fig.7: First derivatives of the experimental TGA curves (red curves) of CZP30-45-60 with the three domains of reduction. Open circles point to the mean temperature (°C) as given by a Gaussian fit (yellow dot curves). The associated number of lost oxygen is given relative to 2.

We focus only on the temperature region upper than 300 °C (after elimination of water and carbonates adsorbed at the surface) and below 600 °C. For each composition, the TGA curves derivatives are modeled using a simple Gaussian decomposition and we determine a mean temperature, a standard deviation and the associated oxygen loss for each domain (Table 4). For all compounds, at most three domains are visible which

can globally be grouped depending on the mean activation temperature at *ca.* 400°C, 440 °C and 550 °C. We assume that the first mechanism, at low temperature, is the continuation of the depletion observed after the synthesis in air, *e.g.* the first mechanism for CZP60 deals with the initial loss of 5% plus the 6.67% appearing within the first peak at 377 °C, *i.e.* 11.67%. The idea for the assignment is then to consider the sequential and preferential depletion of some specific oxygen sites depending on their cation environment.

	Initial oxygen non stoichiometry	Domain 1 $\overline{T}$ (σ) in °C and oxygen loss (%)		Domain 2 $\overline{T}$ (σ) in °C and oxygen loss (%)		Domain 3 $\overline{T}$ (σ) in °C and oxygen loss (%)	
CZP10*	0.85% + …	387 (25)	0.68%			544 (39)	1.98%
Possible environment		0.96% **Pr_2CeZr** / $PrCeZr_2$				3.84% **Ce_2Zr_1** / Pr_2Ce_2	
CZP30*	2.48% + …	405 (26)	3.05%	435 (20)	2.39%	552 (28)	2.00%
Possible environment		6.48% **Pr_2CeZr** / $CePr_3$		2.16% $PrCeZr_2$ / Ce_2Zr_2		2.16% $PrCeZr_2$ / **Ce_2Zr_2**	
CZP45*†	2.15% + …	407 (40)	7.33%	456 (19)	0.94%	539 (24)	0.88%
Possible environment		10.94% **Pr_2CeZr** / $PrCe_2Zr$		2.43% **Pr**$CeZr_2$		1.22% **Ce_2Zr_1** / Pr_2Zr_2	
CZP60*	5.00% + …	378 (30)	6.67%	456 (29)	5.06	550	ε
Possible environment		12.96% **Pr_2CeZr** / Pr_4		6.48% $PrCe_2Zr$ / $PrCe_3$		0.12% $CeZr_3$; 0.54% **Ce_2Zr_1**	
CZP40†	4.90% + …	401 (41)	3.93%	440 (22)	0.81%	536 (44)	2.37%
Possible environment		10.24% Pr_3Zr / Ce_2Zr		1.28% **Pr**Zr_3 / $CeZr_3$		3.84% **Ce_2Zr_1** / Pr_2Zr_2	
CZP33†	4.67% + …	376 (34)	1.54%	417 (19)	1.04%	556 (36)	4.06%

Table 4: Initial oxygen non-stoichiometry deduced from magnetic measurement and oxygen losses in three various domains. We assume that the initial oxygen non-stoichiometry and the first oxygen loss are part of the first domain. The possible cation environments are determined best matching each domain size with the occurrence of a specific environment in each compound. All solutions are given.

For each possible environment, its proportion in each compound is calculated using a binomial law: $p_i(N_{Ce}, N_{Pr}, N_{Zr}) = \binom{4}{N_{Ce}} a^{N_{Ce}} \binom{4-N_{Ce}}{N_{Pr}} b^{N_{Pr}} c^{4-N_{Ce}-N_{Pr}}$ with $\sum_i p_i = 1$; here N_A denotes the amount of each cation in the oxygen environment for a composition $Ce_aPr_bZr_cO_{2-\delta}$ with $a+b+c=1$; obviously, p_i shows some symmetry depending on the composition and N_A, then some sites have the same existence probability (see Table S2). We assume that each reduction mechanism is associated with a specific oxygen departure corresponding to a peculiar OM_4 tetrahedron: for each composition, we match the oxygen loss in the domains with the closest proportion p_i; in a first approximation we discard all effects related to clusterization. For example, using again the case of CZP60, we obtain for the first mechanism the closest $p_i = 12.96\%$ for both $Pr_2Ce_1Zr_1$ and Pr_4 and we associate the oxygen release to one of these two sites. Table 4 gathers all the results of these calculations for all compounds.

It is easily seen that some trends emerge, especially for these compounds with a constant Zr rate at 10% (CZP10, 30, 45, 60). In this series, among the possible solutions the first peak consistently relates to a $Pr_2Ce_1Zr_1$ environment, the second one to $Pr_1Ce_{1\ or\ 2}Zr_{2\ or\ 1}$ and the last one systematically to Ce_2Zr_2. This progression obviously obeys some logic. Following the argument given in the magnetic measurements section, Pr^{4+} is the most reducible cation and it is both the majority in the environment involved in the first mechanism and it is also in sufficient amount to compensate for the departure of one oxygen: $OCe_1^{4+}Pr_2^{4+}Zr_1^{4+} \rightarrow \square Ce_1^{4+}Pr_2^{3+}Zr_1^{4+}$. As Pr^{4+} is consumed, its involvement in the reduction process decreases and the site associated with the second mechanism is impoverished with praseodymium (and even fully absent in the case of CZP10): $OCe_{1\ or\ 2}^{4+}Pr_1^{4+}Zr_{2\ or\ 1}^{4+} \rightarrow \square Ce_{1\ or\ 2}^{4+}Pr_1^{3+}Zr_{2\ or\ 1}^{4+}$; we note here that the reaction is to double depending on the involvement of the cerium cation in the reduction process at this stage. Finally, when all Pr^{4+} is consumed, or at least when no more is reducible, a mechanism implying only cerium ions activates: $OCe_2^{4+}Zr_2^{4+} \rightarrow \square Ce_2^{3+}Zr_2^{4+}$. Several points can be highlighted from the analysis at constant Zr rate (10%): (i) although it is quite simple model to compare the amount of available environments to the amount of oxygen leaving the structure, it looks able to evidence several systematic features; (ii) the domains are clearly identified and their mean temperature barely evolve from a compound to the next one; (iii) the role of Pr^{4+} in the reduction process, and especially at low temperature, agrees well with the assumption given upper in the magnetic measurements section concerning the higher reducibility of praseodymium; (iv) at least one zirconium ion consistently appears in the environment of the labile oxygen; (v) it is also interesting to note that while there is most often only one Zr atom in the environments implying also the Pr cations, there are two when only the Ce cations is involved (Ce_2Zr_2). The presence of some Zr^{4+} in the environments of the labile oxygen is actually not surprising: there can be a steric effect with a larger volume given to the host that may enhance its mobility; it is strongly desymmetrizing the polyhedron and probably destabilizing its host; it is highly polarizing and it is likely to stabilize the reduced cations.

These observations can be used to address the more complex cases of the compounds with constant Pr/Ce ratio (CZP33, 40, 45), especially if we remark that the same domains exist in this series (Table 4). We first note for CZP33 that due to the parity in the cations proportion and the symmetry in N_A, number of environments have the same probability of existence (all three with only one specie in the close surrounding at 1.23%, all six 1+3 environments at 4.94%, all three 2+2 at 7.41% and all three 2+1+1 at 14.81%) what makes a direct discrimination between active sites only on the basis of statistics less obvious. The first domain (4.67% + 1.54% = 6.21 %) could be associated to OPr_3Zr following the previous analysis whereas the second and third domains could respectively correspond to OPr_4 (1.04 %) and $OCeZr_3$ (4.06 %). Finally in $Ce_2Zr_2O_7$ / $Pr_2Zr_2O_7$ pyrochore-type phases , a superstructure of fluorite-type network (depicted on Figure S5) obtained after reduction at T=500°C-600°C under Ar/5% H_2 of $Ce_2Zr_2O_8$ [33] oxide, the oxygen vacancy crystallographic site corresponds precisely to $\square CeZr_3$.

<u>Taking into account this statistical approach and based on first principles</u>* DFT calculations, *the analysis of activation energies of* oxygen *vacancy migration in these complex oxides is in progress.

5- Transport properties measured on dense pellets and influence of the composition

The thermal variation of the total conductivity, measured by the four-point probe method on dense pellets annealed at T=1400°C under air, is shown in Figure 8 for CZ and CZP10-

30-45. The total conductivity values at room temperature, T=230°C and T=430°C are given in Table 5. CZ is strongly insulating and its conductivity could not be measured below 300°C. CZP10 also exhibits a typical insulating behavior with σ ranging from *ca* 10^{-9} to 10^{-4} S/cm from RT to 1000 °C. On the other hand, CZP30 and especially CZP45 compounds, which are more Pr-rich, exhibit higher conductivities what is obviously related to some hopping phenomenon involving the localized 4f orbital or the more extended 5d orbital of Pr atoms[34]

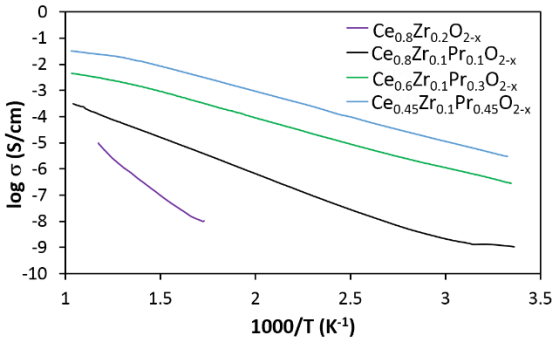

Fig. 8: Thermal variation of the total (ionic + electronic) conductivity measured by four probes method under air between 300K and 1000K for various compositions.

Table 5: Total conductivity values (S/cm) at various temperatures for $Ce_{1-x-y}Zr_xPr_yO_{2-z}$ compounds (see table 1 for oxides formulae) measured by four-probe methods. The error bars of conductivity values and deduced activation energies are less than 1% .

Oxide	Total conductivity at RT (S/cm)	Total conductivity at 230°C (S/cm)	Total conductivity at 430°C (S/cm)
CZ	-	$5*10^{-8}$	$2.3*10^{-7}$
CZP10	$1*10^{-9}$	$6.6*10^{-7}$	$2.6*10^{-5}$
CZP30	$3*10^{-7}$	$8.8*10^{-5}$	$1.2*10^{-3}$
CZP45	$3*10^{-6}$	$9.3*10^{-4}$	$1.2*10^{-2}$

It is worth noting that for both CZP30 and CZP 45, the log (σ) = f (1000 / T) curves evidence two distinct regimes with a clear break in the slopes at *ca* 500 °C. For both compounds, the associated activation energies are 0.38 eV below 500 °C and 0.17 eV above 500 °C. Such significant reduction in the activation energy suggests a change either in the nature and/or the amount of charge carriers. A change of the transport mechanism can also be expected. The thermal variation of the Seebeck coefficient α (Figure 9) measured on a sintered pellet of CZP45 oxide (calcinated at 1400°C under air) reveals this change with a change in the nature of the charge carriers at 520 °C. At low temperatures, when $Pr^{4+}/Pr^{3+}>1$, α is negative (n-type semiconductor). When the temperature is raised up to 400 °C, the reduction of Pr^{4+} to Pr^{3+} begins and holes become the majority charge carriers at 520 °C when the thermopower becomes positive. The low temperature behavior can be seen like an intraspecy charge hopping with a simple charge transfer equilibrium as $Pr^{4+} + Pr^{3+} \leftrightarrow Pr^{3+} + Pr^{4+}$. On the other hand, at high temperature, both this equilibrium and an interspecies mechanism implying holes transfer from the 2p oxygen band (valence band) like $Pr^{4+} + O^{2-} \leftrightarrow Pr^{3+} + O^{-}$ can be also considered.

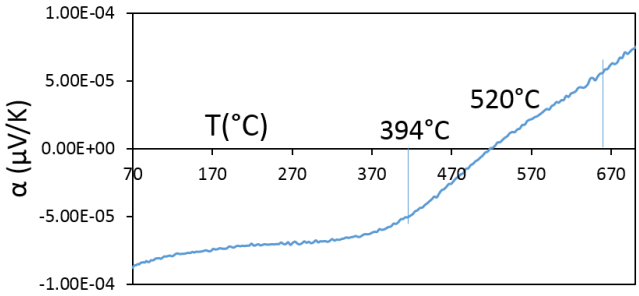

Fig. 9: Thermal variation of the Seebeck coefficient under air of $Ce_{0.45}Zr_{0.1}Pr_{0.45}O_{2-x}$ pellet sintered under air at 1400°C.

An energy band diagram[34] involving the 2p oxygen band, the 4f (Pr^{4+}/Pr^{3+}) levels and the 5d (Ce/Pr) band is schemed in Figure 10.

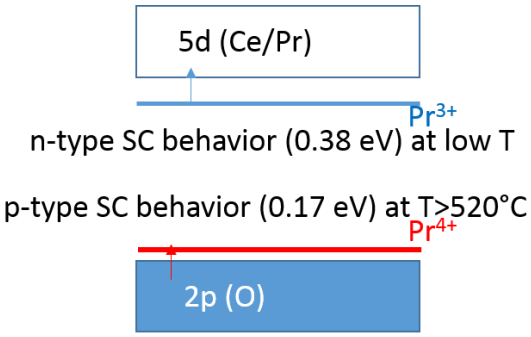

Fig. 10: Band diagram of $Ce_{0.45}Zr_{0.1}Pr_{0.45}O_{2-x}$ complex oxide deduced from the thermal evolution of Seebeck coefficient and total conductivity.

The beginning of the reduction process at 400 °C is confirmed with a TGA experiment carried out under air (Figure S6) using a temperature ramp of 5°C/min, from room temperature up to 800°C on a pellet sintered under air at 1400°C. Fixing $Pr^{4+}/Pr^{3+}=1$ at 520 °C allows calculating the initial Pr^{4+} content in the pellet at 61%, *i.e.* much lower than after a synthesis at only 700 °C. This highlights not only the large range of possible composition but also the high oxygen storage capacity of the compound. Figure S6 also illustrates this point under air and Ar/5%H_2 with plots of the evolution of Pr ions content depending on their valence state (deduced from TGA experiments). Within the same approach, Figure S7 compares all compounds in this study (under Ar/5%H_2), highlighting again the key role of Pr substitution in the low temperature redox process.

6-$^{18}O/^{16}O$ exchange (IEDP-SIMS) and relaxation conductivity measurement on dense pellets

Isotopic Exchange Depth Profile (IEDP) measurements have been performed on dense pellets with CZ, CZP10, CZP30 and CZP45 compositions, after isotopic oxygen exchanges performed at T=400°C during 1h. The oxygen diffusion depth values were initially unknown and the depth profile method (which focuses on few micrometers of analyses only) was first used. The normalized oxygen concentration profiles recorded on CZ and CZP10 pellets are plotted in Figure S8. The

profile recorded on CZ pellet evidences that oxygen has diffused on a very small distance (less than 1µm), while for CZP10, the diffusion is about 4 times larger. At the end of the oxygen profile the natural ^{18}O abundancy is reached. In both cases, the oxygen concentration at depth = 0µm (surface) is very low (around $1.5x10^{-2}$), then from a qualitative point of view, the oxygen surface exchange coefficient is very low. For CZP30 and CZP45 pellets, the oxygen concentration is almost linear as a function of depth (not shown). This means that the diffusion depth is larger than 5µm and thus that the depth profile method is not adapted. Fitting the experimental data with the Crank model[25] leads to determine the D* and k* coefficients on CZ and CZP10 oxides at 400°C (Table 6). Both materials can be considered as bad ionic oxygen conductors with low oxygen surface exchange coefficients.

Table 6: D_{chem}, D*, k_{chem} and k* coefficients determined on CZ, CZP10 and CZP45 materials at different temperature.

Composition	D_{chem} (cm^2/s)	D* (cm^2/s	k_{chem} (cm/s)	k* (cm/s)
CZ (400°C)		$1.2x10^{-13}$		$8.4x10^{-11}$
CZP10 (400°C)		$1x10^{-11}$		$9x10^{-10}$
CZP45 (20°C)		$4x10^{-10}$		$5x10^{-10}$
CZP45 (400°C)	$2x10^{-6}$	$1.5x10^{-8}$ (calculated)	$5x10^{-5}$	
CZP45 (700°C)	$6x10^{-6}$	$4.6x10^{-8}$ (calculated)	$4x10^{-4}$	

In order to obtain the oxygen diffusion profile on a CZP45 pellet, the line scan analysis method has been used. The preliminary oxygen isotopic exchange was performed at T=500°C during 30 minutes. The result is plotted on Figure 11 and is unexpected: instead of the usual progressive decrease of the oxygen concentration from the surface to the bulk, a "reverse" profile is observed, with a larger oxygen concentration in the center of the pellet compared to a value about 10 times lower on the surface.

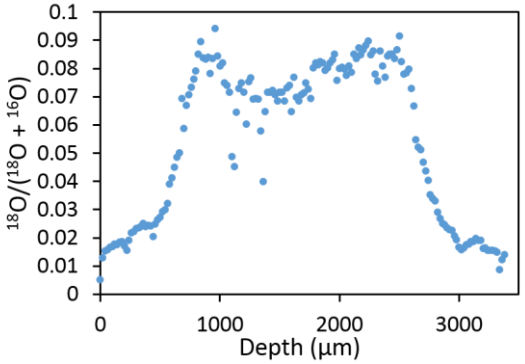

Fig. 11: Normalized oxygen concentration profile recorded on dense pellet with $Ce_{0.45}Zr_{0.1}Pr_{0.45}O_{2-x}$ composition, after a preliminary ^{18}O exchange performed at T=500°C during 30 min.

Experiments were double checked first using the same SIMS device and then using two different devices; the data are perfectly reproducible. In the center of the probed edge, the oxygen concentration is quite low, however 50 times larger than the natural ^{18}O abundancy. At this stage, one can then conclude that CZP45 oxide is a good oxygen ionic conductor, since ^{18}O crossed the entire thickness of the pellet (about 3 mm) in only 30 min. Occurrences of oxygen diffusion across mechanical failures of the pellet are discarded, because in that case huge increases of the oxygen concentration would be observed and only limited thicknesses (few micrometers of the failures) would be concerned. A hypothesis to explain the results stands in the one month delay between the isotopic exchange and the profile recording (because of restricted access to the SIMS device): if the oxygen diffusion coefficient is not zero at room temperature, then, before the measurement, an ^{18}O "retro-diffusion" process can occur from the bulk towards the surface We have modeled the "reverse" profile assuming that ^{18}O was diffusing at 20°C during one month and the order of magnitude of the D* and k* coefficients was determined, *i.e.* $D^*_{CZP45} \sim 4.10^{-10}$ $cm^2.s^{-1}$ and $k^*_{CZP45} \sim 5.10^{-10}$ $cm.s^{-1}$ (Table 6). Both values are high as compared to known room temperature data. At the end of this first part it's only possible to conclude that CZP45 is a good ionic conductor.

Electronic conductivity relaxation measurements have also been performed to get more information on the CZP45 sample. The same pellet was used for several measurements at different temperature. The experimental profiles as well as the models are plotted for the experiments performed at 400 and 700°C. As expected, the electronic conductivity decreases when changing the atmosphere from air to argon, in agreement with the lessening of the charge carrier concentration. The profile, represented on Figure S9, can be globally modeled using the solution of the diffusion equation given by Crank[25], meaning that the experimental process is governed both by the surface exchange and the oxygen diffusion phenomena. At low temperature (400°C), the model is in good agreement with the experimental data, while there is more discrepancy at high temperature (700°C). Such difference may arise from the experimental conditions during which the applied oxygen partial pressure step (10^{-1} (air) ~ 10^{-5} (argon)) is probably slightly too strong, and the expected linear evolution of the measured conductivity as a function of the oxygen concentration is not fully ensured. However, an order of magnitude of both D_{chem} and k_{chem} has been obtained at T=400 and 700 °C and the results are gathered in Table 6. These results evidenced that CZP45 oxide is a very good oxygen ionic conductor even at 400°C. D* and k* coefficients are for instance comparable to the ones which can be extrapolated from the high temperature values determined on the best SOFC cathode materials[35,36]. D* and k* coefficients largely increase when the temperature is increased from 400 to 700°C. The comparison of the D_{chem} and D* coefficients is possible using the thermodynamic factor γ given by the relations:

$$D^* = D_{chem}/\gamma \text{ and } \gamma = d\ln(pO_2)/2d\ln(C_o)$$

where C_o is the oxygen concentration in the material. It was determined by TGA measurements as a function of temperature, either under air and argon, leading to determine γ ~ 130. The corresponding calculated D* coefficients are given in Table 6. The evolution of log(D*) *vs.* 1000/T is plotted in Figure 12 for the measurements performed at three temperatures using either $^{18}O/^{16}O$ exchange or relaxation conductivity measurement. A typical temperature activated process is evidenced with $E_a \approx 37$ meV. It would be necessary to get additional measurements, especially considering various oxygen partial pressure.

However this study leads to get quite accurate ionic diffusion data for CZP45 oxide and to conclude without any doubt that this material is a very good oxygen conductor, in particular in the low temperature range.

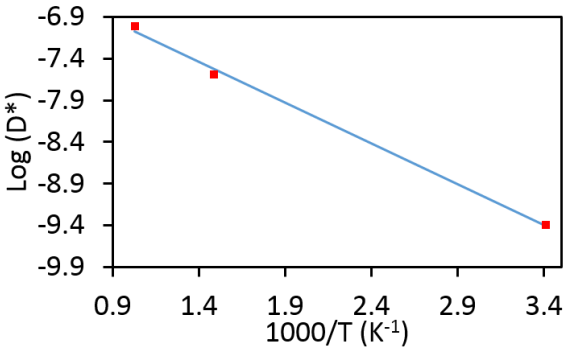

Fig.12: Thermal evolution of D* oxygen tracer self-diffusion coefficient of $Ce_{0.45}Zr_{0.1}Pr_{0.45}O_{2-x}$ oxide.

CONCLUSION

Several compositions were carefully selected, then investigated in details in the pseudo-ternary CeO_2-ZrO_2-PrO_x phase diagram. We focused on two series either at constant Zr content (10%) or equal Ce and Pr content. We show that the thermal stability of these materials is ensured up to about T=1400°C. We globally observe that the higher the Zr content, the lower the Pr^{4+} rate. At 10 molar% Zr, the Pr^{4+} rate fixes around 66%, like in Pr_6O_{11}, except for $Ce_{0.45}Zr_{0.1}Pr_{0.45}O_{2-x}$ (CZP45) which exhibits the highest Pr^{4+} rate peaking at 81% just after annealing at T=700°C under air. The presence of Pr, more reducible than Ce, globally shifts the redox process at low temperature. This is particularly visible for compositions with high Pr content. The presence of Zr appears to enhance the Ce reducibility and to decrease the Ce^{4+} reduction temperature. For oxides containing as much Ce as Pr, such as CZP45, the Pr^{4+} reduction first occurs, followed by that of Ce^{4+} at higher temperature. Furthermore, the increase of Pr content ($Ce_{0.3}Zr_{0.1}Pr_{0.6}O_{2-x}$ = CZP60) also allows enhancing the Ce^{4+} reducibility at low temperature. Intra-atomic charge transfer equilibria such as $Pr^{4+} + Pr^{3+}/Ce^{3+} \leftrightarrow Pr^{3+} + Pr^{4+}/Ce^{4+}$ and $Pr^{4+}/Ce^{4+} + O^{2-} \leftrightarrow Pr^{3+}/Ce^{3+} + O^-$ should contribute to the reducible Pr^{4+}/Ce^{4+} regulation rate in the CZP series. The Pr^{4+}/Ce^{4+} reduction step can be systematically associated to an oxygen release and especially to the most labile oxygen environments.

The most probable labile oxygen sites, selected on the basis of a multinomial law that follows the released oxygen rate during the first annealing under air at T=700°C and in addition during the first reduction step under Ar/H_2 (T<500°C) may contain systematically one Zr atom, two Pr and one Ce atoms as first neighbors. The combination of two various rare earths (Ce/Pr) with various valences and polarizabilities and in addition one Zr^{4+} as smaller and more polarizing cation should contribute to a strong distortion of the oxygen tetrahedral sites. Then, the oxygen departure should be followed by the complete Pr^{4+} reduction on this specific site: $OCe_1^{4+}Pr_2^{4+}Zr_1^{4+} \rightarrow \square Ce_1^{4+}Pr_2^{3+}Zr_1^{4+}$. As the Ce/Pr atomic ratio is equal to 1 with a low Zr content (CZP45 versus CZP60 and CZP30), the Pr^{4+} amount of the pristine material before reduction remains the highest. The two main charge transfer equilibria, $Pr^{3+} + Ce^{4+} \leftrightarrow Pr^{4+} + Ce^{3+}$ and $Ce^{3+} + O^- \leftrightarrow Ce^{4+} + O^{2-}$ in the vicinity of the most labile oxygen ($OZrPr_2Ce$ in CZP45) should explain such a behavior in order to maintain a high level of Pr^{4+}. As mentioned in the introductive part, the stabilization of Pr^{4+}/Pr^{3+} mixed valences is associated with the creation of oxygen vacancies in the $Pr_{1-x}Zr_xO_{2-y}$ series ($0.02 < x < 0.5$) and the local environment is strongly affected by the presence of Pr^{3+} as well as the formation of oxygen vacancies in the vicinity of Zr atom [14]. In the CeO_2-ZrO_2-PrO_x phase diagram, the redox properties are indeed related to the O/Zr local environments.

Pr-poor compounds are insulating (CZ, CZP10) but high Pr content (CZP30, CZP45, CZP60) enhances the electrical conductivity and the materials become rather good semiconductors with lower activation energies. Two temperature domains are evidenced from electronic transport properties with at low temperature, a n-type conduction (E_a=0.38 eV) and at high temperature (>520 °C) a p-type behavior (E_a=0.17 eV). The change of the nature of charge carriers is related to the partial reduction of Pr^{4+} ions under air starting at T=400°C. Then two charge transfer equilibria, $Pr^{3+} + Pr^{4+} \leftrightarrow Pr^{4+} + Pr^{3+}$ (e^- electron transport) and $Pr^{4+} + O^{2-} \leftrightarrow Pr^{3+} + O^-$ (h^+ holes transport) may occur at low and high temperature, respectively. The magnitude of the D* oxygen tracer self-diffusion coefficient of CZ, CZP10 and CZP45 was estimated at T=400°C from two independent measurements (IEDP and electronic conductivity relaxation). It strongly varies with the Pr content from 10^{-13} $cm^2.s^{-1}$ (CZ) to 10^{-11} $cm^2.s^{-1}$ (CZP10) and 10^{-8} $cm^2.s^{-1}$ (CZP45). This evidences in particular a very good oxygen diffusion in CZP45 with a very high coefficient as compared to other good ionic conductors, especially at such low temperature. The reducibility and OSC properties of CZP series are comparable with the literature[3, 4, 5, 22] with the best redox properties obtained for CZP45. The preparation of dense pellets sintering at 1400°C under air with the control of phase stability allows to measure accurately the transport properties and for the first time to estimate the high oxygen tracer self-diffusion coefficient in CZP45 sample.

ASSOCIATED CONTENT

Supporting Information.

The following file are available free of charge (Word document) via the internet at http : //pubs.acs.org.

Figures S1 shows the powder XRD patterns of $Ce_{1-x-y}Zr_xPr_yO_{2-z}$ annealed at 1400°C under air. Figure S2 shows the thermal expansion behavior of CZP33 and CZP45 oxides. Figure S3 shows STEM light field image (left) analysis and EDX elementary analyses of CZP10 complex oxide (right, "three colors" images obtained by addition of the three elementary cartographies). Figure S4 shows the temperature dependence of the magnetic susceptibility χ and the inverse $1/\chi$ for the $Ce_{0.45}Zr_{0.1}Pr_{0.45}O_{2-z}$ compound annealed at 700°C under air (experiments and fittings with the Curie-Weiss law). Figure S5 shows the oxygen vacancies ordering in $Pr_2Zr_2O_7$ Pyrochlore-type structure and the deduced oxygen vacancy environment ($\square Zr_3Pr$ site) in the related fluorite-type network. Figure S6 shows TGA under air (speed rate : 5°C/min) performed on a

$Ce_{0.45}Zr_{0.1}Pr_{0.45}O_{2-x}$ pellet (sintered under air at 1400°C) and the estimation of Pr^{4+}/Pr^{3+} molar concentration evolution versus temperature under air and Ar/H_2. Figure S7 shows the estimation (from TGA measurements under Ar/H_2) of Pr^{4+}/Pr^{3+} molar concentration evolution versus temperature. Figure S8 shows the normalized oxygen concentration profiles recorded on dense pellets with CZ (left) and CZP10 (right) compositions, after a preliminary ^{18}O exchange performed at T=400°C during 1h. Figure S9 shows the electronic conductivity relaxation profiles (experiments and fittings), recorded on CZP45 complex oxide and performed at 400°C and 700°C. Table S1 shows the initial Pr^{4+} rates, Δm/m, deduced ΔO exchanged oxygen and final TR^{4+}/TR^{3+} molar contents after reduction (TGA- Ar/5% H_2, or H_2/TPR- Ar/1%H_2) of complex oxides $Ce_{1-x-y}Zr_xPr_yO_{2-z}$ (see Table 1 for oxides formulae) annealed at T = 700 °C under air. Table S2 shows the probabilities for various local oxygen environments in CZP complex oxides deduced from multinomial law calculation (see table 1 for oxides formulae).

AUTHOR INFORMATION

Corresponding Author

* alain.demourgues@icmcb.cnrs.fr

Author Contributions

The manuscript was written through contributions of all authors. / All authors have given approval to the final version of the manuscript.

Funding Sources

The authors thank the PSA and SOLVAY companies for financial support.

REFERENCES

1. Trovarelli, A. Catalysis by ceria and related materials. (*Imperial College Press*, **2005**).
2. Kaspar, J.; Fornasiero, P.; Hickey. N, Automotive catalytic converters : current status and some perspectives. .*Catal. Today* **2003**, *77*, 419-449.
3. Bensaid, S.; Piumetti, M.; Novara, C.; Giorgis, F.; Chiodoni, A.; Russo, N.; Fino, D. Catalytic oxidation of CO and soot over Ce-Zr-Pr mixed oxides synthesized in a multi-inlet vortex reactor: effect of structural defects on the catalytic activity. *Nano Res. Lett.* **2016,** *11(1)*, 494**.**
4. Andana, T.; Piumetti, M.; Bensaid, S.; Russo, N.; Fino, D.; Pirone, R. CO and soot oxidation over Ce-Zr-Pr oxide catalysts. *Nano Res. Lett.* **2016**, *11(1)*, 278
5. Sinev, M. Y.; Graham, G. W.; Haack, L. P.; Shelef, M. Kinetic and structural studies of oxygen availability of the mixed oxides $Pr_{1-x}M_xO_y$ (M = Ce, Zr). *J. Mater. Res.* **1996**, *11***,** 1960–1971.
6. Rohart, E.; Verdier, S.; Demourgues, A.; Harlé, V.; Pacaud, B.; Baylet, A.; Takemori, H.; Suda, E.; Allain, M. New CeO_2-ZrO_2 mixed oxides with improved redox properties for advanced TWC catalysts. *SAE Technical Paper*. **2006.**
7. Thomson, J. B.; Armstrong, A. R.; Bruce, P. G. A new class of pyrochlore solid solution formed by chemical intercalation of oxygen. *J. Am. Chem. Soc.* **1996**, *118***,** 11129–11133.
8. Sasaki, T.; Ukyo, Y.; Kuroda, K.; Aral, S; Muto, S.; Saka, H. Crystal structure of $Ce_2Zr_2O_7$ and β-$Ce_2Zr_2O_{7.5}$. *J. Ceram. Soc. Jpn.* **2004**, *112(8)*, 440-444.
9. Tolla, B.; Demourgues, A.; Isnard, O.; Menetrier, M.; Pouchard, M.; Rabardel, L.; Seguelong, T.; Structural investigation of oxygen insertion within the $Ce_2Sn_2O_7$–$Ce_2Sn_2O_8$ pyrochlore solid solution by means of in situ neutron diffraction experiments. *J. Mater. Chem.* **1999**, *9***,** 3131–3136.
10. Muroi, T.; Echigoya, J.; Suto, H. Structure and phase diagram of ZrO_2–CeO_2 ceramics. *Trans. Jpn. Inst. Met*. **1988**, *29***,** 634–641.
11. Von Dreele, R. B.; Eyring, L.; Bowman, A. L.; Yarnell, J. L. Refinement of the crystal structure of Pr_7O_{12} by powder neutron diffraction. *Acta Cryst. B* **1975,** *31***,** 971–974.
12. Eyring, L. The binary rare earth oxides. *Handb. Phys. Chem. Rare Earths* **1979,** *3*, 337–399.
13. Zhang, J.; Von Dreele, R. B.; Eyring, L. Structures in the oxygen-deficient fluorite-related RnO_{2n-2} homologous series: $Pr_{12}O_{22}$. *J. Solid. State Chem*. **1996,** *122*, 53–58.
14. Abel, J.; Lamirand-Majimel, M.; Majimel, J.; Bellière-Baca, V.; Harlé, V.; André, A.; Prestipino, C.; Figueroa, S.; Durand, D.; Demourgues, A. *et al.* Oxygen non-stoichiometry phenomena in $Pr_{1-x}Zr_xO_{2-y}$ compounds ($0.02 < x < 0.5$). *Dalton Trans* **2014,** *43*, 15183–15191.
15. Wang, W.; Lin, P.; Fu, Y.; Cao, G. Redox properties and catalytic behavior of praseodymium-modified (Ce-Zr)O_2 solid solutions in three-way catalysts. *Catal. Lett*. **2002,** *82*, 19–27.
16. Ran, R.; Weng, D.; Wu, X.; Fan, J.; Wang, L.; Wu, X. *et al.* Structure and oxygen storage capacity of Pr-doped $Ce_{0.26}Zr_{0.74}O_2$ mixed oxides. *J. Rare Earths* **2011,** *29*, 1053–1059.
17. Fagg, D.; Kharton, V.; Shaula, A.; Marozau, I.; Frade, J. Mixed conductivity, thermal expansion, and oxygen permeability of Ce(Pr,Zr)O. *Sol. Stat. Ion.* **2005**, *176*, 1723–1730.
18. Fagg, D. P.; Frade, J. R.; Kharton, V. V.; Marozau, I. P. The defect chemistry of Ce(Pr, Zr)$O_{2-\delta}$. *J. Solid State Chem.* **2006,** *179*, 1469–1477.
19. Kharton, V. V.; Viskup, A. P.; Figueiredo, F. M.; Naumovich, E. N.; Yaremchenko, A. A.; Marques, F. M. B. Electron-hole conduction in Pr doped Ce(Gd)$O_{2-\delta}$ by faradaic efficiency and emf measurements. *Electroch. Acta.* **2001**, *46*, 2879-2889.
20. Kim, J. J.; Bishop, S. R.; Thompson, N. J.; Chen, D.; Tuller, H. L. Investigation of non-stoichiometry in oxide thin films by simultaneous *in situ* optical absorption and chemical capacitance measurements: Pr-doped Ceria, a case study. *Chem. Mater.* **2014,** *26*, 1374–1379.
21. Sravan, K.; K. B.; Deshpande, P. A. On identification of labile Oxygen in Ceria-Based Solid Solutions: Which Oxygen Leaves the Lattice? J. Phys. Chem. C **2015,** *119*, 8692–8702.
22. Rossignol, S.; Descorme, C.; Kappenstein, C.; Duprez, D. Synthesis, structure and catalytic properties of Zr–Ce–Pr–O mixed oxides. *J. Mater. Chem.* **2001,** *11*, 2587–2592.
23. De Souza, R. A.; Zehnpfenning, J.; Martin, M.; Maier, J. Determining oxygen isotope profiles in oxides with time-of flight SIMS. *Solid State Ionics*. **2005,** *176*, 1465–1471.
24. Bassat, J.-M.; Petitjean, M.; Fouletier, J.; Lalanne, C.; Caboche, G.; Mauvy, F.; Grenier, J. C. Oxygen isotopic exchange: A useful tool for characterizing oxygen conducting oxides. *Appl. Catal. Gen.* **2005,** *289*, 84–89.
25. Crank, J. The mathematics of diffusion. (Clarendon Press, **1976**).
26. Hernández-Velasco, J. Unusual magnetic behaviour in Sr2PrO4. *J. Magn. Magn. Mater.* **2007,** *310*, 1669–1671.
27. Hatnean, M. C.; Sibille, R.; Lees, M. R.; Kenzelmann, M.; Ban, V.; Pomjakushin, V.; Balakrishnan, G. Single crystal growth, structure and magnetic properties of $Pr_2Hf_2O_7$ pyrochlore. *J. Phys. Condens. Matter* **2017,** *29*, 75902.
28. Matsuhira, K.; Sekine, C.; Paulsen, C.; Wakeshima, M.; Hinatsu, Y.; Kitazawa, T.; Kiuchi, Y.; Hiroi, Z.; Takagi, S. Spin freezing in the pyrochlore antiferromagnet $Pr_2Zr_2O_7$. *J. Phys. Conf. Ser.* **2009,** *145*, 12031.
29. Porter, S. H.; Huang, Z.; Cheng, Z.; Avdeev, M.; Chen, Z.; Dou, S.; Woodward, P. M. Structural and magnetic properties of RTiNO2 (R=Ce, Pr, Nd) perovskite nitride oxides. *J. Solid State Chem*. **2015,** *226*, 279–285.

30. Malchus, M.; Jansen, M. Electrocrystallization of PrO_2 and TbO_{2-x} from alkali hydroxide melts and characterization of the fluorite-related TbO_{2-x}. *Solid State Sci.* **1998,** *2*, 65–70.
31. Aruna, S. T.; Kini, N. S.; Shetty, S.; Rajam, K. S. Synthesis of nanocrystalline $CeAlO_3$ by solution-combustion route. *Mater. Chem. Phys.* **2010,** *119*, 485–489.
32. Hatnean, M. C.; Decorse, C.; Lees, M. R.; Petrenko, O. A.; Keeble, D. S.; Balakrishnan, G. Structural and magnetic properties of single-crystals of the geometrically frustrated zirconium pyrochlore, $Pr_2Zr_2O_7$. *Mater. Res. Express* **2014,** *1*, 26109.
33. Alessandri, I.; Banares, M. A.; Depero, L. E.; Ferroni, M.; Fornasiero, P.; Gennari, F. C.; Hickey, N.; Martinez-Huerta, M. V.; Montini, T. Structural investigation of $Ce_2Zr_2O_8$ after redox treatments which lead to low temperature reduction. *Top. Catal.* **2006,** *41*, 35–42.
34. Lal, H. B.; Gaur, K. Electrical conduction in non-metallic rare-earth solids. *J. Mater. Sci.* **1988,** *23*, 919–923.
35. B.C.H. Steele and J.M. Bae, Properties of $La_{0.6}Sr_{0.4}Co_{0.2}Fe_{0.8}O_{3-x}$ (LSCF) double layer cathodes on gadolinium-doped cerium oxide (CGO) electrolytes: II. Role of oxygen exchange and diffusion, *Solid State Ionics* 1998, *106*, 255-261.
36. M. Burriel, H. Tellez, R.J. Chater, R. Castaing, P. Veber, M. Zaghrioui, T. Ishihara, J.A. Kilner and J.M. Bassat Influence of crystal orientation and annealing on the oxygen diffusion and surface exchange of $La_2NiO_{4+\delta}$, *J. Phys. Chem. C*. 2016, *120*, 17927-17938.

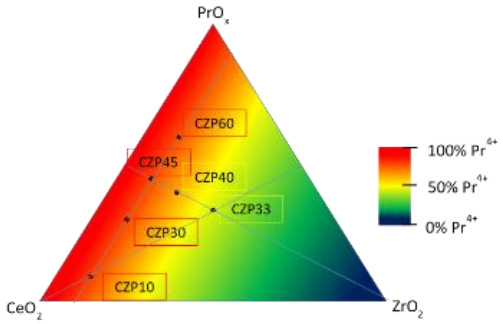

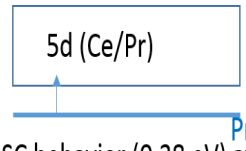

n-type SC behavior (0.38 eV) at low T

p-type SC behavior (0.17 eV) at T>520°C